RSC Advances

ROYAL SOCIETY OF CHEMISTRY

www.rsc.org/advances

Cite this: DOI: 10.1039/c0xx00000x

www.rsc.org/xxxxxx

ARTICLE TYPE

A Novel Hydrothermal Synthesis and Characteristics of Porous Mn_3O_4 for Supercapacitor with High Rate Capability

Fengyu Yang,[a] Minshou Zhao,[*a,b] Qujiang Sun[a] and Yuqing Qiao[a]

Received (in XXX, XXX) Xth XXXXXXXXX 20XX, Accepted Xth XXXXXXXXX 20XX

DOI: 10.1039/b000000x

Porous nanostructured Mn_3O_4 particles were successfully synthesized by a novel hydrothermal method via adding the surfactant of hexadecyltrimethylammonium bromide (CTAB). They were characterized by the techniques of thermogravimetric and differential thermal analysis (TG/DTA), X-ray diffraction (XRD), field emission scan electron microscope (SEM), transmission electron microscope (TEM), N_2-adoportion. Electrochemical performance of the sample was studied by the galvanostatic charge-discharge, cyclic voltammetry and electrochemical impedance spectroscopy in 1 M Na_2SO_4 aqueous solution electrolyte. It exhibits a high specific capacitance (232.5 F g^{-1} at 0.5 A g^{-1}) and good rate capability (190 F g^{-1} at 5 A g^{-1}), which can be attributed to its porous structure, the defects and vacancies on the surface. The capacitance retention reaches to 78% after 5000 cycles at a current density of 5 A g^{-1}. The results show that Mn_3O_4 has the potential to be used as the electrode material for a supercapacitor with the high performances.

Introduction

In the 21st century, the rapid development of the economy and social great progress require many kinds of energy storage and conversion devices, and more research of alternative energy storage and conversion devices is critical. Supercapacitor has attracted much attention for its high power density, excellent reversibility and long cycling life[1]. On the basis of the energy storage mechanism, supercapacitor can be divided into two kinds, namely, electrochemical double-layer capacitors(EDLCS) stored energy between the electrode and electrolyte interfaces simply via ion adsorption and desorption, and pseudo-capacitor which undergo a fast and reversible Faradaic reaction[2,3]. Always, the transition metal oxides present high specific capacitance from both double-layer capacitances and pseudo-capacitances, and have bright prospective in the future. Thus, it is of great significance to carry out the research of transition metal oxides used as the supercapacitor electrode material.

Among the various transition metal oxides, manganese oxides (MnOx) have been investigated as the most promising electrode material[4-6], because they are low-cost and environmentally kindly while still provide a large theoretical capacitance. Pang *et al*[7]. have synthesized a Cu–MnO_2 composite which has a high specific capacity of 1024 F g^{-1} at 1.5 A g^{-1}. As far as we know, only a few reports[8-11] were related to the electrochemical capacitive properties of Mn_3O_4.

It has been noted that the electrochemical capacitive behavior of nanomaterial strongly depends on the size, shape, and the porosity of internal structure[12,13]. Herein, we employ a novel solvent for the hydrothermal method and a surfactant-assistant strategy, a cooperative self-assembly of inorganic species and surfactants to synthesize the mesoporous Mn_3O_4. When the as-obtained Mn_3O_4 is used as supercpacitor electrode material, it exhibits a high specific capacitance (232.5 F g^{-1} at 0.5 A g^{-1}), a good rate capability (190 F g^{-1} at 5 A g^{-1}), and the capacitance retention reaches to 78% after 5000 cycles at a current density of 5 A g^{-1}.

Experimental

Sample preparation

In a typical synthesis of Mn_3O_4, 0.2g hexadecyltrimethylammonium bromide (CTAB) dissolved in N, N-Dimethylformamide(DMF) with stirring for 1 h to form a stable solution. Then 0.01 mol of $Mn(CH_3COO)_2 \cdot 4H_2O$ was added into the above solution. Followed by stirring for 1 h, 0.6 g urea was introduced into the solution. Until the reactant dissolved completely, the mixed solution was transferred to a Teflon-lined stainless steel autoclave (100mL) and heated in an electric oven at 140 ℃ for 4 h. The resultant was separated by vacuum filtration, washed with DI water and ethanol, and dried at 60 ℃ under vacuum for 8 h. Mn_3O_4 obtained was heated at 300 ℃ for 5 h in air atmosphere. For comparison, samples without the surfactant of CTAB(WS-Mn_3O_4) were also prepared using the similar route.

Material characterization

X-ray diffraction(XRD) pattern of the sample was recorded by RIGAKU D/max-2500 using Cu K_α radiation (λ=0.15406 nm) at 40 kV and 100 mA. The patterns were obtained in 2θ ranges between 10° and 90° at a scanning rate of 4°/min. SEM was performed on a field emission Hitachi S-4800 instrument operating at an accelerating voltage of 10 kV. TEM was

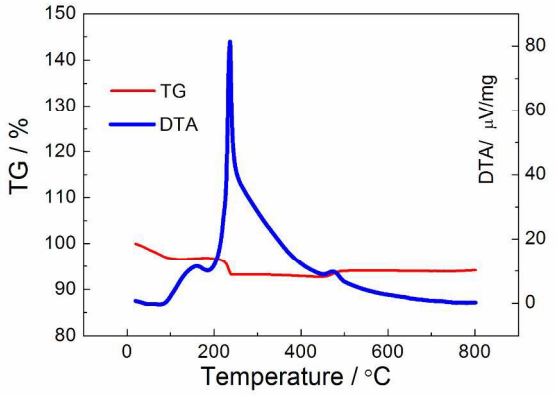

Fig.1 Thermogravimetric and differential thermal analysis

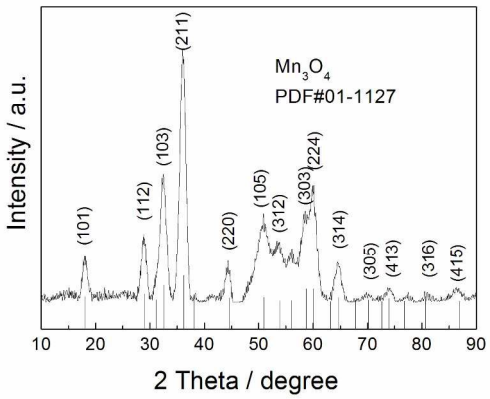

Fig.2 XRD pattern of Mn_3O_4 nanoparticles

performed using Hitachi HT7700 instrument with a field emission gun operating at 200 kV to examine the morphologies. Nitrogen adsorption measurements were performed on a Micromeritics ASAP 2020 adsorption analyzer. Specific surface areas were calculated by the Brunaure-Emmert-Teller (BET) method. Pore volumes and sizes were estimated from the pore size distribution curves from the adsorption isotherms using the Barrett-Joyner-Halenda (BJH) method. TG/DTA was performed at a heating rate of 4 ºC in flowing air by the Japanese Matsu Atsu analysis workstation TA-60WS.

Preparation of electrode

The working electrodes of Mn_3O_4 were prepared as follow. Primarily, Mn_3O_4 (70 wt. %), polyvinylidenefluoride (a binder, 10 wt. %) and acetylene black (20 wt. %) was mixed in N-methyl pyrrolidinone, grinded for half an hour in a mortar, thus the slurry was obtained and then was coated on a foam nickel plate about 1 cm^2, and the plate was dried at 120 ºC under vacuum, the coating weight was fixed about 1 mg.

Electrochemical characterization

The electrochemical performance of Mn_3O_4 was examined by CV, galvanostatic charge and discharge measurement. Cyclic voltammetry measurements were performed on a CHI660E electrochemical workstation. Galvanostatic charge and discharge measurements were carried on a Neware BTS-5V10mA multi-channel battery testing system. The electrochemical cell was a three electrode configuration, the above plate attached to a nickel wire as working electrode, a platinum plate as a counter electrode and a saturated calomel electrode (SCE) as the reference electrode. All the electrochemical measurements were carried out in 1 M Na_2SO_4 electrolyte. CV measurement was performed over the potential range of 0 to 1.0 V at the scan rate of 1, 5, 10, 50 and 100 mV s^{-1}, respectively. Galvanostatic charge/discharge curves were measured at different current densities from 0.5 to 5 A g^{-1}. Electrochemical impedance spectroscopy was also performed on a CHI660E electrochemical workstation over a frequency range from10^5 to 0.1 Hz.

Results and discussion

Structures characterization

The porous Mn_3O_4 nanoparticles were prepared by a hydrothermal reaction, followed by a thermal annealing, and the annealing temperature is critical for controlling the phase, morphology and crystallinity of the final resultant of reaction[14], which will have much influence on the capacitive properties. Therefore, we have studied the thermal-annealing behavior of the precursor under air atmosphere. The thermogravimetric and differential thermal analysis curves are shown in Fig.1. The weight loss below 100 ℃ corresponds to the loss of remaining ethanol and adsorbed water in the precursor, and the weight loss in the temperature region of 200-245 ℃ is related to the formation of Mn_3O_4, while the weight gain in the temperature region of 460-510 ℃ corresponds to the phase conversion. The DTA curve shows a small exothermic peak at 160.02 ℃, which is related to the decomposition of trace surfactant CTAB. The obvious peak, located at 236.98 ℃, is also related to the formation of Mn_3O_4, and another smaller peak is located at 472.28 ℃, where a solid-state reaction occurs with the phase transformation. While further increasing temperature, the TG curve almost keeps a constant value until 800 ℃. Referred to the related paper[15], finally we determined the annealing temperature is 300 ℃.

The structure and phase of the sample was characterized by X-ray diffraction, as shown in Fig 2. All peaks could be indexed to a tetragonal Hausmannite Mn_3O_4 with space group I41/amd (PDF #01-1127). No other crystalline phases were observed. Hausmannite Mn_3O_4 crystal structure has been observed from the XRD pattern, and the peak positions agree well with the PDF card no.01-1127 with 18.02°, 29.02°, 32.53°, 36.00°, 44.04°, 50.46°, 53.78°, 56.30°, 60.08°, 64.64°, 70.06°, 74.01°, 80.70° and 86.95° at 2θ, which correspond to the (101), (112), (103), (211), (220), (105), (312), (303), (224), (314), (305), (413), (316), and (415) planes of body centered tetragonal manganese oxide for the Mn_3O_4 nanoparticles, respectively. From the width of diffraction peaks and using the Scherrer equation, we estimate a nanoparticle size of around 10 nm.

Morphology characterization

The morphology of the Mn_3O_4 nanoparticles was investigated by FESEM and TEM. Fig. 3a and b shows the SEM images of the Mn_3O_4 nanoparticles. These images present a partially attached particle structure and almost uniform spherical shape nanoparticles. Because the size of the particle is so small, about

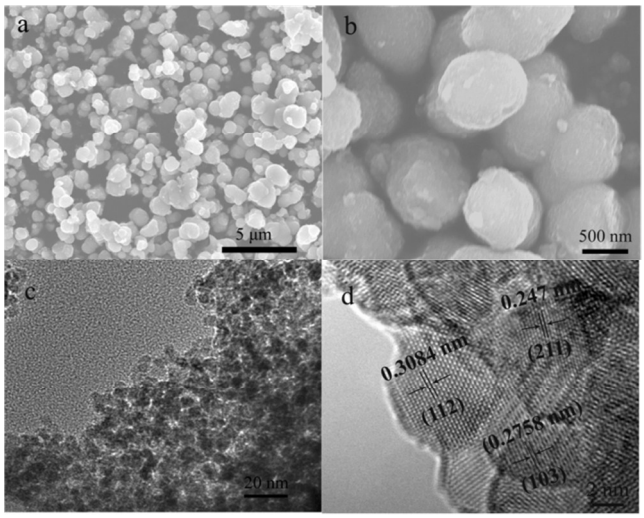

Fig.3 (a) SEM of low magnification (b) SEM of high magnification (c) TEM and (d) HRTEM images of Mn_3O_4 nanoparticles

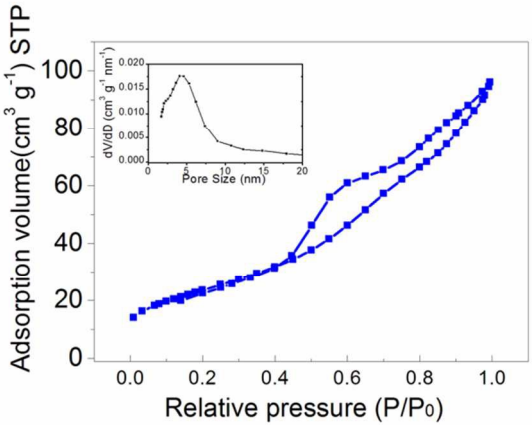

Fig.4 N_2 adsorption–desorption isotherms of synthesized Mn_3O_4 and mesopore size distribution curve of Mn_3O_4 (in inset)

10 nm, that it is liable to aggregate to spherical particles, which look to be larger in the Fig. 3b. Also, there are some vacancies and defects on the surface of the sphere, thus, it seems to be unsmooth. It is probably due to the effect of the CTAB surfactant micelle, which provides the soft template and can decompose to result in porous structure. The vacancies and defects are beneficial to the electron transport and redox reaction, which can improve the electrochemical performance of the Mn_3O_4 as the supercapacitor electrode material to some extent. Fig. 3c shows the TEM images of the Mn_3O_4 nanoparticles. From the images, we could observe the size of a particle is about 9 nm, which is in accord with the result come from the Scherrer equation. The formation of uniform nanoparticles can also be noted in the images, and the uniform structure helps in efficient electron transport at the interface of the electrode/electrolyte Fig. 3d is a high-resolution transmission electron microscopy (HR-TEM) image of the nanoparticles, from which the lattice fringes of Mn_3O_4 can be identified in [211], [103] and [112] planes with matching d-spacing of 0.247, 0.276 and 0.308 nm, respectively[16]. WS-Mn_3O_4 samples are charaterized for comparison also, whose shape and size are in random, Also the aggregation terribly occured among the particles (Supplementary Fig. S1).

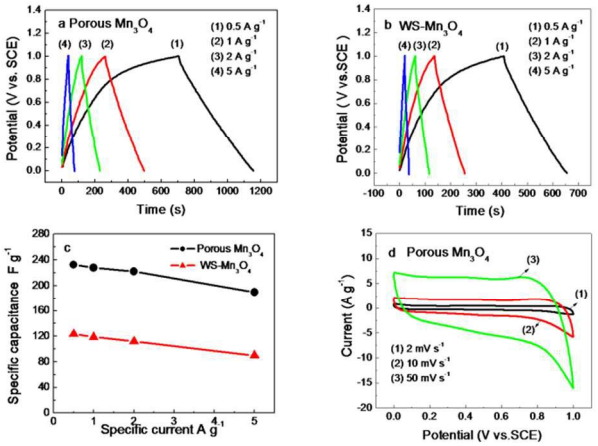

Fig.5 (a) Charge and discharge curve of porous Mn_3O_4 at different current densities (b) Charge and discharge curve of WS-Mn_3O_4 at different current densities (c) Current density versus specific capacitance curve (d) Cyclic voltammograms of porous Mn_3O_4 electrode at different scan rates

The pore size distribution and surface area of Mn_3O_4 samples are examined by nitrogen adsorption-desorption method. The isotherm profiles are shown in Fig. 4. It shows that Mn_3O_4 nanoparticles have a type IV adsorption/desorption curve with hysteresis loop which is characteristic of mesoporous materials. The BET surface area of the Mn_3O_4 sample is measured to be 86.172 m^2 g^{-1} and a total pore volume of 0.150 cm^3 g^{-1}. The pore-size distribution curve (the inset in Fig.4) shows a size distribution centered at 5 nm, which is more suitable for the supercapacitors with aqueous neutral electrolytes[17]. The narrow pore size distribution and relative bigger volume contribute to the effective electron transport at the interface of electrode/electrolyte.

Meanwhile, The BET surface area of WS-Mn_3O_4 is 33.97 $m^2g^{-1}$and the total pore volume is 0.096 cm^3 g^{-1}(Supplementary Fig. S2).

Electrochemical properties of porous Mn_3O_4

The potential of the porous Mn_3O_4 sample as the supercapacitor electrode material was evaluated by galvanostatic charge-discharge technique and cyclic voltammetry. The WS-Mn_3O_4 samples are also examined for comparison. For the galvanostatic charge-discharge measurements, the potential window was set at 0.0-1.0 V vs. SCE, with 1 M Na_2SO_4 solution serving as the electrolyte, and the results are shown in Fig. 5. The charge-discharge curves demonstrate the intrinsic nature of pseudocapacitance for the porous Mn_3O_4 and WS-Mn_3O_4, i.e. the longer discharging time and the higher specific capacitance. The specific capacitances of the electrode can be estimated from the discharge curves according to the following equation: $C = I \triangle t/ m \triangle V$ where C (F g^{-1}) is the specific capacitance, I (A g^{-1}) is the discharging constant density, $\triangle t$ (s) is the discharging time, m (g) is the mass of the active material in the working electrode, $\triangle V$ (V) is the potential window taken in the test[18,19].

In the Fig. 5a, at the current density of 0.5, 1, 2, 5 A g^{-1}, the obtained reversible specific capacitance of the porous Mn_3O_4 has reached to 232.5, 228, 222 and 190 F g^{-1}, respectively, matching with those of the composite of the Mn_3O_4 with carbon or graphene[20-22], overwhelming those of the Mn_3O_4 synthesized by

other methods[10,16] . In the Fig. 5b, the corresponding values of WS-Mn_3O_4 are merely 123.5, 119, 112 and 90 F g^{-1}. Fig. 5c makes a comparison of the specific capacitance between the porous Mn_3O_4 and WS-Mn_3O_4, It is evident that the porous Mn_3O_4 has crushing advantages over WS-Mn_3O_4. Also, the results indicate the porous Mn_3O_4 nanoparticles serving as the electrode material have high rate capacitance, which is one of the most important electrochemical parameters for the application of supercapacitor, especially for the electric vehicle[23,24]. The high rate performance of capacitance of Mn_3O_4 is probably ascribed to the small size, porous structure and the vacancies and defects on the surface of the spherical nanoparticles. Due to Mn_3O_4 particles are in nano-size with the diameter of 9 nm as well as the relatively high surface area of the nanoparticles[25], considerable amount of Mn_3O_4/electrolyte contact areas could be created. Furthermore, the vacancies and defects acting as the active site can facilitate the redox reaction, thus increasing the specific capacitance.

Fig. 5d shows the cyclic voltammograms ~~and the scan rate versus specific capacitance.~~ The applied potential of the system varied in the range of 0.0 to 1.0 V vs. SCE at a scan rate of 1, 2, 5, 10 and 50 mV s^{-1}. The tests were conducted in 1 M Na_2SO_4 solution. As shown in Fig. 5d, the curve profiles have an approximate rectangular shape and symmetric current–potential characteristics between 0 to 1.0 V, indicating capacitive behaviour through the 1.0 V voltage window in the Na_2SO_4 solution[26]. At the scan rates of 1, 2, 5, 10 and 50 mV s^{-1}, the corresponding specific capacitances were 236.86, 219.60, 196.77, 173.29 and 115.6 F g^{-1}, respectively. With increasing the scan rate, a decrease in the capacitance occurs, which may due to the ion transport. Usually at the higher scan rate, the ions do not have enough time to diffuse into the interface of electrode /electrolyte.

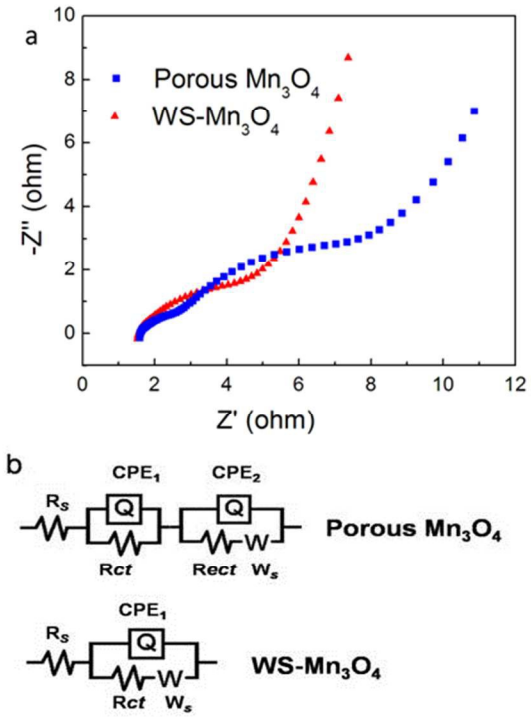

Fig. 6 (a) Nyquist plots for porous Mn_3O_4 and WS-Mn_3O_4 electrode (b) equivalent circuit

To investigate the features of the ions and electron transport within the capacitive electrode, electrochemical impedance spectra(EIS) was performed at open circuit potential over the frequency range 0.1~100,000 Hz with the amplitude of 5 mV. Fig.6a shows the Nyquist plots. The EIS data can be fitted by Zview software according to an equivalent circuit mainly consisting of a bulk solution resistance R_s, charge-transfer R_{ct}, constant phase element(CPE) and Warburg resistance(W_s), as shown in Fig. 6b. At high frequency region, the intercept at real axis(R_s) corresponds to the electrolyte resistance, the values for the two samples are almost the same around 0.58 Ω. A semicircle near high frequency region can be observed, and the diameter of the semicircle corresponds to the charge transfer resistance(R_{ct}) at the interface of electrode/electrolyte. The charge-transfer resistance R_{ct} was calculated to be 0.91 and 4.87 Ω, for the porous Mn_3O_4 and WS-Mn_3O_4 electrode, respectively. It is obvious that charge-transfer resistance at the porous Mn_3O_4 electrode dramatically reduces compared with the WS-Mn_3O_4 electrode. Another semicircle in the middle-frequency region can be seen in the Nyquist plot of the porous Mn_3O_4 electrode, which perhaps implies a more complicated electrochemical process occurs, but we can't give satisfactory explanation up to now. The resistance resulted from the ions diffusion is known as Warburg resistance(W_s). The slope of the straight line at low frequency region gives a semi-qualitative result of Warburg resistance. It can be seen that the slope of the straight line for WS-Mn_3O_4 electrode is much larger than that for the porous Mn_3O_4 electrode, indicating a lower diffusive resistance at the interface of electrolyte/ the porous Mn_3O_4 electrode.

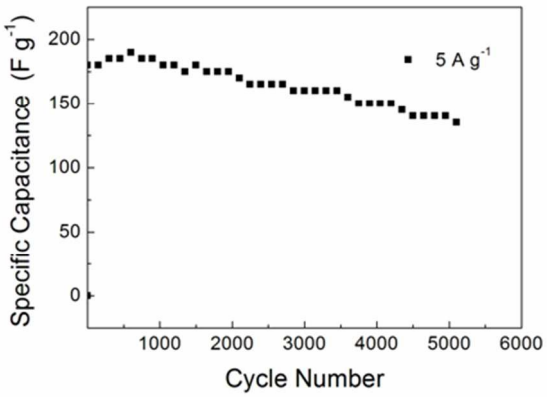

Fig.7 Cycling stability profile for Mn_3O_4 electrode at a current density of 5 A g^{-1}

The stability of the electrode with cycling is of great significance for the practical applications of the supercapacitors[27]. The cyclic stability test has been carried out by the galvanostatic charge-discharge technique at a constant density of 5A g^{-1} in the potential range of 0.0 to 1.0 V for 5000 cycles. The specific capacitance as a function of cycle numbers is presented in Fig. 7. During the first 600 cycles, the specific capacitance increases continuously, because the electrochemical activation commonly occurs in front electrochemical process[28,29], and then, the degradation in specific capacitance slowly occurs, capacitance

retention of 78% is kept until 5000 cycles. This indicates that the Mn_3O_4 nanoparticles taken as the electrode material are activated at the initial stage and keep relatively stable state in the following cycles.

Conclusions

Porous nanostructured Mn_3O_4 particles were successfully synthesized by a novel hydrothermal method via adding the surfactant CTAB. The porous Mn_3O_4 material exhibits a high specific capacitance of 232.5 F g^{-1} at 0.5 A g^{-1} and good rate capability of 190 F g^{-1} at 5 A g^{-1}, which can be attributed to its porous structure and the defects and vacancies on the surface. The capacitance retention reaches to 78% after 5000 cycles at a current density of 5 A g^{-1}. These results show that the porous Mn_3O_4 is a promising candidate as an electrode material of supercapacitor.

Notes and references

[a] *College of Environmental and Chemical Engineering,Yanshan University, Qinhuangdao 066004, China.Tel.: +86 18733569006 ;E-mail address: zhaoms@ysu.edu.cn*

[b] *State Key Laboratory of Metastable Material Science and Technology, Yanshan University, Qinhuangdao 066004, China.*

1 C. Wei, H. Pang, B. Zhang, Q. Lu, S. Liang and F. Gao, *Sci Rep*, 2013, **3**, 2193.
2 G. Yu, X. Xie, L. Pan, Z. Bao and Y. Cui, *Nano Energy*, 2013, **2**, 213.
3 A. Davies, P. Audette, B. Farrow, F. Hassan, Z. Chen, J.-Y. Choi and A. Yu, *J. Phys. Chem. C*, 2011, **115**, 17612.
4 L. Li, Z. Hu, Y. Yang, P. Liang, A. Lu, H. Xu, Y. Hu and H. Wu, *Chin. J. Chem.*, 2013, **31**, 1290.
5 W.-Y. Ko, L.-J. Chen, Y.-H. Chen, W.-H. Chen, K.-M. Lu, J.-R. Yang, Y.-C. Yen and K.-J. Lin, *J. Phys. Chem. C*, 2013, **117**, 16290.
6 W. Yan, T. Ayvazian, J. Kim, Y. Liu, K. C. Donavan, W. Xing, Y. Yang, J. C. Hemminger and R. M. Penner, *Acs Nano*, 2011, **5**, 8275.
7 H. Pang, S. Wang, G. Li, Y. Ma, J. Li, X. Li, L. Zhang, J. Zhang and H. Zheng, *J. Mater. Chem. A*, 2013, **1**, 5053.
8 H. Jiang, T. Zhao, C. Yan, J. Ma and C. Li, *Nanoscale*, 2010, **2**, 2195.
9 D. Li, F. Meng, X. Yan, L. Yang, H. Heng and Y. Zhu, *Nanoscale Res. Lett.*, 2013, **8**, 1.
10 D. Yan, Y. Li, Y. Liu, R. Zhuo, Z. Wu, B. Geng, J. Wang, P. Ren, P. Yan and Z. Geng, *Mater. Lett.*, 2014, **117**, 62.
11 H. Pang, J. Deng, J. Du, S. Li, J. Li, Y. Ma, J. Zhang and J. Chen, *Dalton Trans*, 2012, **41**, 10175.
12 C. Yuan, H. B. Wu, Y. Xie and X. W. D. Lou, *Angew. Chem. Int. Ed.*, 2014, **53**, 1488.
13 F. Wang, H. Dai, J. Deng, G. Bai, K. Ji and Y. Liu, *Environ. Sci. Technol*, 2012, **46**, 4034.
14 G. An, P. Yu, M. Xiao, Z. Liu, Z. Miao, K. Ding and L. Mao, *Nanotechnology*, 2008, **19**, 275709.
15 J. Gao, M. A. Lowe and H. D. Abruna, *Chem. Mater.*, 2011, **23**, 3223.
16 M. Fang, X. Tan, M. Liu, S. Kang, X. Hu and L. Zhang, *CrystEngComm*, 2011, **13**, 4915.
17 S. Nagamuthu, S. Vijayakumar and G. Muralidharan, *Energy & Fuels*, 2013, **27**, 3508.
18 K.-S. Kim and S.-J. Park, *Bull. Korean Chem. Soc*, 2013, **34**, 2343.
19 G. S. Gund, D. P. Dubal, B. H. Patil, S. S. Shinde and C. D. Lokhande, *Electrochim. Acta*, 2013, **92**, 205.
20 Y. Zhao, W. Ran, D.-B. Xiong, L. Zhang, J. Xu and F. Gao, *Mater. Lett.*, 2014, **118**, 80.
21 Y. Fan, X. Zhang, Y. Liu, Q. Cai and J. Zhang, *Mater. Lett.*, 2013, **95**, 153.
22 J. W. Lee, A. S. Hall, J.-D. Kim and T. E. Mallouk, *Chem. Mater.*, 2012, **24**, 1158.
23 R. Quintero, D. Y. Kim, K. Hasegawa, Y. Yamada, A. Yamada and S. Noda, *RSC Advances*, 2014, **4**, 8230.
24 H. Xia, B. Li and L. Lu, *RSC Advances*, 2014, **4**, 11111.
25 B. Wang, J. Park, C. Wang, H. Ahn and G. Wang, *Electrochim. Acta*, 2010, **55**, 6812.
26 S. Bao, W. Jia and M. Xu, *Rare Met.*, 2011, **30**, 81.
27 L. Zhu, S. Zhang, Y. Cui, H. Song and X. Chen, *Electrochim. Acta*, 2013, **89**, 18.
28 Y. H. Lin, T. Y. Wei, H. C. Chien and S. Y. Lu, *Adv Energy Mater.*, 2011, **1**, 901.
29 Y. Wu, S. Liu, H. Wang, X. Wang, X. Zhang and G. Jin, *Electrochim. Acta*, 2013, **90**, 210.